Journal of Materials Chemistry C

PAPER

View Article Online
View Journal | View Issue

Cite this: J. Mater. Chem. C, 2016, 4, 9331

Structural, optical, magnetic, ferroelectric, and piezoelectric properties of (Pb,Ba)(Ti,Fe)O_3 perovskites: a macroscopic and nanoscale properties approach

F. M. Pontes,*[a] A. J. Chiquito,[b] W. B. Bastos,[c] Marcelo A. Pereira-da-Silva[de] and E. Longo[cf]

Received 26th August 2016,
Accepted 12th September 2016

DOI: 10.1039/c6tc03704f

www.rsc.org/MaterialsC

Single-phase $Pb_{0.50}Ba_{0.50}Ti_{1-x}Fe_xO_3$ (PBTF) polycrystalline thin films with different Fe doping contents were prepared on Pt/Ti/SiO_2/Si substrates using a chemical solution deposition method. The effects of doping on their structural, optical, magnetic, and electrical properties were studied *via* a multi-technique approach on different scales. A structural phase transition from tetragonal to pseudocubic was observed when the Fe content increased, resulting in tetragonality reduction of the thin films. Another consequence of the Fe content increase was the decrease in the optical band gap energy, probably induced by localized states within the forbidden gap of the PBTF thin films associated with structural disorder. The Fe addition also resulted in a gradual modification of the domain structure, as clearly observed by piezoresponse force microscopy. Two processes, a weakened distortion of the TiO_6 sublattice and a decreased ferroelectric and piezoelectric response, were identified. At the macroscopic level, the ferroelectric properties of the films decreased with increasing Fe content, in good agreement with the nanoscale piezoresponse force microscopy data. Finally, a long-range magnetic order to ferromagnetism evolved by increasing the Fe doping content from x = 0.0 to 0.10.

Introduction

In recent years, researchers have been conducting useful research on the ABO_3 perovskite family. Due to the new ferroelectric and ferromagnetic properties that some ABO_3 perovskite-family members simultaneously exhibit after doping, a renewed interest has been devoted to Bi-based solid solutions.[1–3] Alternatively, the best known example of the doped ABO_3 perovskite-family is the $PbTiO_3$ prototype of classical ferroelectrics, which can be engineered to fit a wide range of applications. This occurs when a partial, or even complete replacement of the Pb atom (A-dodecahedral atomic site) by specific dopants, such as Ca, Sr, Ba, La, and Co, and/or replacement of the Ti atom (B-octahedral atomic site) by Zr, Fe, Cu, Sc, Ni, and Mn, occurs.[4–9] In light of this compositional engineering research, the prediction of material properties from the chemical composition is a primary goal of materials science for the development of new high-tech devices; therefore, it is expected that the doped ABO_3-based solid solution (compositional engineering) displays remarkably different structures, and electronic and electrical properties, either in nanoscale or microscopic dimensions. Hence, chemical doping/substitution is viewed as a challenge for compositional engineering, for tailoring specific properties (optical, magnetic, sensors, catalysts, solar cells, dielectric, ferroelectric, piezoelectric, pyroelectric, *etc.*) of the ABO_3-based perovskite family.[10–14] For example, Fuflyigin *et al.*[15] studied the electro-optic effect in $Pb_xBa_{1-x}TiO_3$ (PBT) thin films. The PBT thin films were shown to be transparent over a wider wavelength range (350–2000 nm), which offers the possibility for using them as light-controlling devices. Lee *et al.*[16] realized fundamental research on structural transformation in $Pb_xBa_{1-x}TiO_3$ (PBT) nanoparticles. Recently, Tyablikov *et al.* reported a novel perovskite compound ($Pb_{2.4}Ba_{2.6}Fe_2Sc_2TiO_{13}$) with an ordered arrangement of different B-cations along the {110} perovskite planes, synthesized using a citrate-based route.[17] Brehm *et al.*, reported some physical and electronic properties of hypothetical $PbTiO_3$-based oxysulfides,

[a] Department of Chemistry, Universidade Estadual Paulista – Unesp, P.O. Box 473, 17033-360, Bauru, São Paulo, Brazil. E-mail: fenelon@fc.unesp.br; Fax: +55 14 3103 6088; Tel: +55 14 3103 6135
[b] NanO LaB – Department of Physics, Universidade Federal de São Carlos, Via Washington Luiz, Km 235, P.O. Box 676, 13565-905, São Carlos, São Paulo, Brazil
[c] Institute of Chemistry, Universidade Estadual Paulista – Unesp, Araraquara, São Paulo, Brazil
[d] Institute of Physics of São Carlos, USP, São Carlos, 13560-250, São Paulo, Brazil
[e] UNICEP, São Carlos, 13563-470, São Paulo, Brazil
[f] LIEC – Department of Chemistry, Universidade Federal de São Carlos, Via Washington Luiz, Km 235, P.O. Box 676, 13565-905, São Carlos, São Paulo, Brazil

$PbTiO_{3-x}S_x$, by first principles calculations.[18] The theoretical analysis indicates that the compounds should be considered as candidates for solar bulk photovoltaic material. As reported by Zhao *et al.*, Co-doped $PbTiO_3$ thin films showed reduced ferroelectricity accompanied by enhanced ferromagnetism.[19] Ren *et al.* reported ferroelectric and ferromagnetic properties for $Pb(Ti_{1-x}Fe_x)O_3$ nanoparticles prepared by hydrothermal synthesis.[20] In addition, Bai *et al.* reported the preparation of highly (100)-oriented $Pb(Zr_{0.5}Ti_{0.5})O_3$ thin films with different Fe doping concentrations, and observed that the dielectric constant of the 1% Fe-doped PZT sample was significantly higher than that of the 2% Fe-doped sample.[21] Furthermore, it has been exhaustively reported that chemical doping/substitution of foreign elements into a perovskite structure can lead to the formation of various local defects in the host lattice. Remarkably, the presence of defects, such as dislocations and vacancies (oxygen and cation) can directly influence the magnetic or ferroelectric polarization response at the nanoscale level, including domain wall dynamics, nucleation, *etc.* In particular, one of the most important methods of investigating the electric polarization process at the nanoscale level is piezo-response force microscopy (PFM).[22–26] Ferrarelli *et al.*[27] reported a systematic decrease in piezoelectric response for $Ba_{1-x}Dy_xTi_{1-x}Sc_xO_3$ ceramics with increasing x. Recently, Yang *et al.*[28] reported extensively on the role of defects on the ferroelectric domain nucleation and growth process, using PFM-based experimental studies. In addition, PFM was extensively used by Gobeljic *et al.*[29] to study the evolution of the piezoelectric response and local hysteresis loops for $0.93Bi_{0.5}Na_{0.5}TiO_3$–$0.07BaTiO_3$ and $0.92Bi_{0.5}Na_{0.5}TiO_3$–$0.06BaTiO_3$–$0.02K_{0.5}Na_{0.5}NbO_3$ composites. Recently, Yu *et al.* investigated the ferroelectric domain evolution of tetragonal $Pb(Zr_xTi_{1-x})O_3$ thin films on $SrTiO_3$(100) substrates by PFM.[30]

Therefore, in this study, we systematically investigated the influence of the Fe doping concentration on the structural, microstructural, dielectric, ferroelectric, magnetic, and optical properties of $(Pb_{0.50}Ba_{0.50})(Ti_{1-x}Fe_x)O_3$ (PBTF) thin films synthesized using the polymeric precursor method. In particular, PFM was carried out to investigate in detail both the domain structure evolution and the local ferroelectric polarization switching behavior as a function of the sample composition. Finally, we compared the nanoscale measurements carried out by PFM with the macroscopic polarization experimental data.

Experimental procedure

Barium acetate $[Ba(C_2H_3O_2)_2]$, lead acetate trihydrate $[Pb(CH_3CO_2)_2{\cdot}3H_2O]$, iron nitrate $[Fe(NO_3)_3{\cdot}9H_2O]$, and titanium isopropoxide $Ti[OCH(CH_3)_2]_4$ were used as precursor materials for Ba, Pb, Fe, and Ti, respectively. Initially, $Ti[OCH(CH_3)_2]_4$ was dissolved in a mixture of deionized water and citric acid at 80 °C under magnetic stirring. Separately, $[Fe(NO_3)_3{\cdot}9H_2O]$ was also dissolved in a mixture of deionized water and citric acid at 80 °C under magnetic stirring. The Ti–citrate and Fe–citrate solutions were mixed at a stoichiometric ratio to produce a $Ti_{1-x}Fe_x$ solution at 80 °C under constant stirring. Then, lead acetate trihydrate was dissolved in deionized water and added drop-by-drop under constant stirring to the $Ti_{1-x}Fe_x$ solution to produce a Pb–Fe–Ti complex solution. After homogenization, barium acetate was slowly added under constant stirring, resulting in a clear Pb–Ba–Ti–Fe complex solution. In addition, a small amount of citric acid was added to increase the stability of the polymeric network structure. Finally, 40 wt% of ethylene glycol monomer was added (based on the final product) to the $(Pb_{0.50}Ba_{0.50})(Ti_{1-x}Fe_x)O_3$ complex solution. The solution was stirred constantly at 90 °C until a transparent and stable colorless, light-yellow, yellow, and light-brown precursor complex solution was obtained for x = 0.0, 1.0, 5.0, and 10.0 mol% Fe doping, respectively. These solutions were somewhat viscous, but without visible phase separation. The precursor solution was deposited on the $Pt/Ti/SiO_2/Si$ and quartz substrates by spin coating at 6000 rpm for 20 s using a spinner (spin-coater KW-4B, Chemat Technology) and a syringe filter to avoid particulate contamination.

After spin coating, the samples were pre-heated at 200 °C for 10 min on a hot plate to remove the residual solvent. Then, the thin films were annealed layer by layer at 400 °C for 4 h, and 700 °C for 2 h (heating rate of 5 °C min^{-1}) under air to remove residual organic components and crystallize the sample, respectively. The thin films were prepared by repeating the deposition and pyrolysis/crystallization cycles.

The phase structures of the $(Pb_{0.50}Ba_{0.50})(Ti_{1-x}Fe_x)O_3$ samples were identified using a Rigaku MiniFlex600 X-ray diffractometer (XRD, CuK_α radiation, λ = 1.54056 Å). The thickness of the thin films was measured using a field-emission scanning electron microscope (FE-SEM, FEG-VP Zeiss Supra 35) with a secondary electron lens detector on a freshly fractured film/substrate cross-section. The optical transmittance of the $(Pb_{0.50}Ba_{0.50})(Ti_{1-x}Fe_x)O_3$ thin films was recorded in the 200–1100 nm wavelength range using a Perkin Elmer Lambda 1050 spectrophotometer.

A LabRAM HR Evolution micro-Raman spectrometer from Horiba Scientific was used to perform the Raman measurements, while the thin films were maintained at room temperature. The 532 nm line of the Nd:YAG laser beam was focused using a 100× objective, generating an intensity of 0.9 mW on the sample.

To measure the electrical properties, circular Au electrodes were prepared by evaporation through a shadow mask with a 4.9×10^{-2} mm^2 dot area to obtain an array of capacitors. The deposition was carried out under vacuum (10^{-6} Torr). Ferroelectric and dielectric properties were measured at room temperature using a Precision Premier II system from Radiant Technology (using standard bipolar signal at 2 kHz) and an Agilent 4294A Precision Impedance Analyzer, respectively.

The topography, polarization pattern of ferroelectric domain structures, and local hysteresis loops were investigated at the nanoscale level on ferroelectric thin films using a commercial AFM (MultiMode Nanoscope V, Bruker), modified to be used as a PFM. The system was equipped with a lock-in amplifier (SR850, Stanford) and a function generator (33220A, Agilent). During the PFM measurements, the conductive probe was electrically grounded and an external voltage was applied to

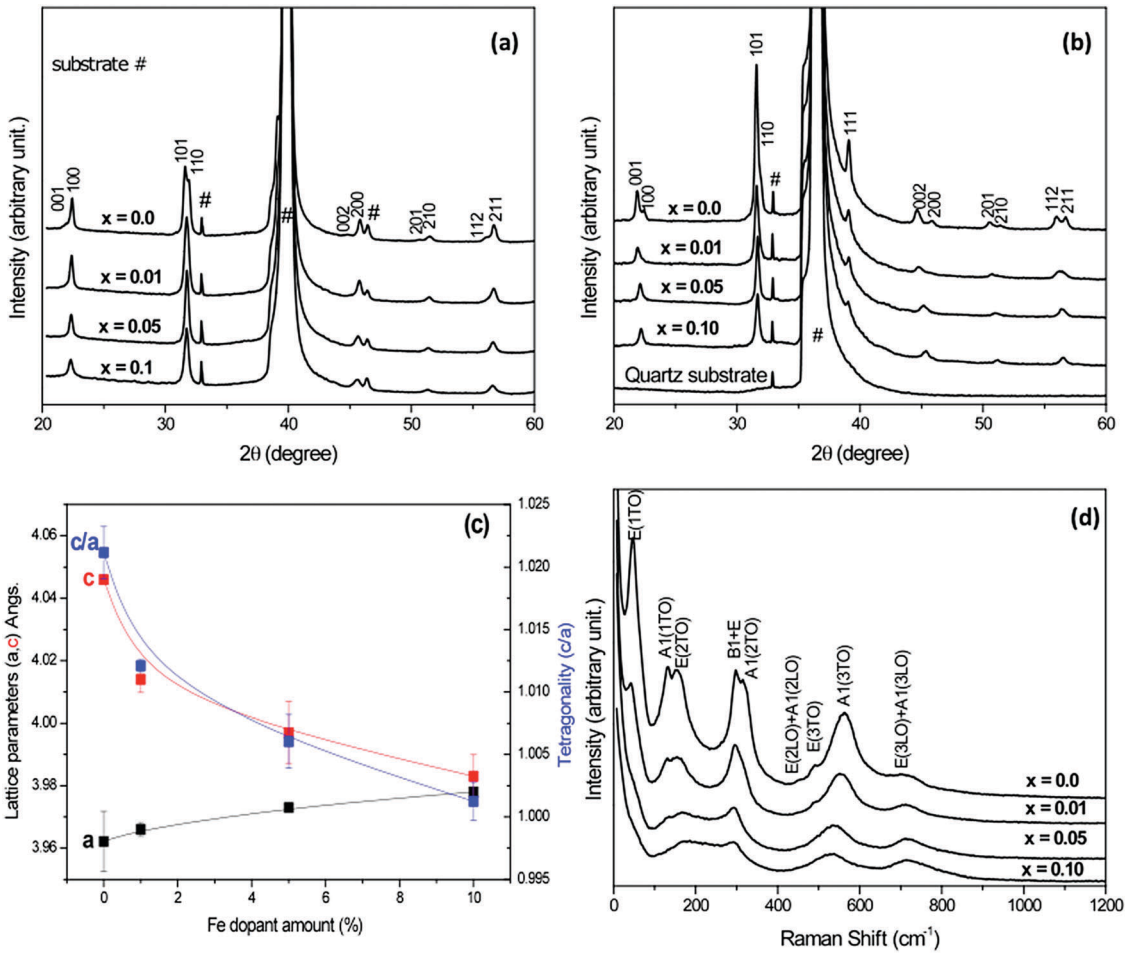

Fig. 1 XRD spectra for the $Pb_{0.50}Ba_{0.50}Ti_{1-x}Fe_xO_3$ thin films grown on (a) $Si/SiO_2/Ti/Pt$ and (b) quartz substrates. (c) Composition-dependent lattice constants (*a*, *c*, and *c*/*a*) for the thin films on $Si/SiO_2/Ti/Pt$ substrates. (d) Raman spectra of the $Pb_{0.50}Ba_{0.50}Ti_{1-x}Fe_xO_3$ thin films grown on $Si/SiO_2/Ti/Pt$.

the bottom Pt electrode operated with a driving amplitude of 1 V (RMS). The magnetic properties were measured at temperatures of 300 K and 10 K, using a vibrating sample magnetometer (MPMS3-SQUID-VSM, Quantum Design).

Results and discussion

The XRD patterns of the undoped PBT and doped PBTF thin films on $Si/SiO_2/Ti/Pt$ and quartz substrates are shown in Fig. 1(a) and (b), respectively. All thin films showed a well-crystallized perovskite phase with no preferred orientations, suggesting a polycrystalline structure after calcination at 700 °C. The undoped PBT thin films clearly revealed splitting of (001)/(100), (101)/(110), and (002)/(200) peaks, confirming the tetragonal structural phase, as shown in Fig. 1(a). Nevertheless, for Fe contents above 1.0 mol%, splitting of the (001)/(100), (101)/(110), and (002)/(200) peaks rapidly decreased and disappeared (below the detection limit of the instrument), suggesting that the tetragonal structural phase became unstable. Thus, the tetragonal instability caused by the Fe ions dissolved in the TiO_6 octahedral structure substituting for Ti ions, produce less distorted TiO_6 octahedral units, which play an important role in ferroelectric properties such as hysteresis loops, phase transition temperatures, and piezoelectric responses. From the XRD patterns, the lattice parameters *a* and *c* were estimated as a function of the different Fe-doped concentrations (Fig. 1(c)). Fig. 1(c) shows that the tetragonality of the thin films decreased significantly with increasing Fe doping, indicating a gradual structural phase transition from tetragonal to cubic at room temperature. Also, Verma[31] and Ganegoda,[32] have established similar tetragonality parameters for this system.

Raman spectroscopy was carried out to provide additional information, since this method is very sensitive to both variations of local bonding and short- and medium-length range symmetry breaking. Raman spectra of the undoped PBT and doped PBTF thin films are shown in Fig. 1(d). The spectrum of the undoped PBT thin films presents the typical signature of a tetragonal perovskite ferroelectric phase, which is also in good agreement with the prototypical ferroelectric $PbTiO_3$.[33] In particular, for the undoped PBT films, the E(1TO) phonon mode, also known as the soft mode, originates from the A ions (A = Pb, Ba) vibrating against the BO_6 (B = Ti, Fe) octahedral structure. The presence of this E(1TO) phonon mode implies a

strongly locally-distorted structure, corresponding to the tetragonal ferroelectric structural phase. According to Freire *et al.*, the locally distorted structure is driven by the mismatch between O and Ti atoms at the B-octahedral site of the ABO_3 perovskite.[34] Accordingly, the suppression of this local distortion by chemical doping/substitution results in a phonon mode shift toward lower wavenumbers with increasing Fe content. A similar phonon mode behavior was reported for polycrystalline $NdFeO_3$–$PbTiO_3$ thin films by Zhao *et al.*[4] By increasing the Fe content, a progressive decrease of the ''soft mode'' occurs, leading to its complete disappearance for $x \geq 5.0$ mol%; this clearly suggests a paraelectric–ferroelectric phase transition at room temperature. In addition, by increasing the Fe doping content, there is a marked shift in the A1(3TO) mode towards lower wavenumbers; this mode corresponds to the movement of B-site ions from the oxygen octahedral cage (BO_6). Freire and Katiyar reported that the A1(3TO) mode was associated with vibrations along the spontaneous polarization vector in the prototype ferroelectric $PbTiO_3$.[34] This indicates that the distortion of the oxygen octahedral cages for the doped PBTF thin films is weakened as the Fe concentration increases. Therefore, Ti ions should occupy most of the symmetrical positions in the octahedral oxygen cage of the perovskite crystal structure, *i.e.*, an off-center to on-center transformation process. In addition, a close inspection of the Raman spectrum showed that the phonon intensity decreased and the line widths became broader with increasing Fe content; *i.e.*, disorder phenomena will broaden the Raman modes.[35] However, in the paraelectric state (for $x \geq 5.0$ mol%), the persistence of Raman-active modes is due to the well-known breaking of selection rules, induced by an inherent lattice disorder, caused by the following: (i) the presence of defects, such as oxygen vacancies; (ii) short and medium-range cationic distortions due to Fe/Ti substitution; (iii) nano- and micro-scale chemical heterogeneity. Although the XRD-based experimental studies suggested the presence of an apparent cubic-like perovskite structure at room temperature for high-doping compositions (Fe $>$ 1.0% mol), Raman studies clearly indicate the presence of a pseudocubic-like perovskite paraelectric phase.

The optical properties of the undoped PBT and doped PBTF thin films with different Fe contents deposited on quartz substrates were investigated by recording the transmission response between 200 and 1100 nm (Fig. 2(a)). The $Pb_{0.50}Ba_{0.50}Ti_{1-x}Fe_xO_3$ film thickness was 260, 240, 240, and 280 nm for x = 0.0, 0.01, 0.05, and 0.10, respectively. Our experimental results for the Fe doping show a red shift of the optical absorption edge, indicating a decrease of the band gap energy. In addition, the band gap energies of the thin films were estimated using Tauc's law:[36,37]

$$\alpha h\nu = A(h\nu - E_g)^n \quad (1)$$

where n is a constant that characterizes the different types of transitions (n = 1/2, 3/2, 2, or 3 for allowed direct, forbidden direct, allowed indirect, and forbidden indirect, respectively); h is the Planck constant; ν is the photon frequency; $h\nu$ is the incident photon energy; α is the absorption coefficient; A is a constant and E_g is the band gap energy value. Thus, a plot of $(\alpha h\nu)^n$ *versus* incident photon energy ($h\nu$) yields the band gap (E_g) value. As shown in Fig. 2(b), the correlation between $(\alpha h\nu)^2$ and ($h\nu$) varies linearly in the high-energy region of the absorption edge, which is consistent with a direct band gap. Based on this process, the band gap energy values were estimated by extrapolating the linear portion of the plot correlating $(\alpha h\nu)^2$ and ($h\nu$) to $(\alpha h\nu)^2 = 0$, as shown by the dotted lines in Fig. 2(b). The band gap energies for the $Pb_{0.50}Ba_{0.50}Ti_{1-x}Fe_xO_3$ thin films were 3.59, 3.55, 3.43, and 3.12 eV when x = 0.0, 0.01, 0.05, and 0.10, respectively. The PBTF band gap energies decreased with increasing Fe doping content (inset of Fig. 2(b)). This is a direct consequence of the band structure (electronic states density) modification from the undoped PBT to the doped PBTF thin films. According to electronic-structure calculations by first-principles methods, the band gap energy of the undoped PBT sample is determined by the difference between the conduction band (CB), containing mainly Ti 3d orbitals, and the valence band (VB), containing mainly O 2p orbitals. Therefore, the

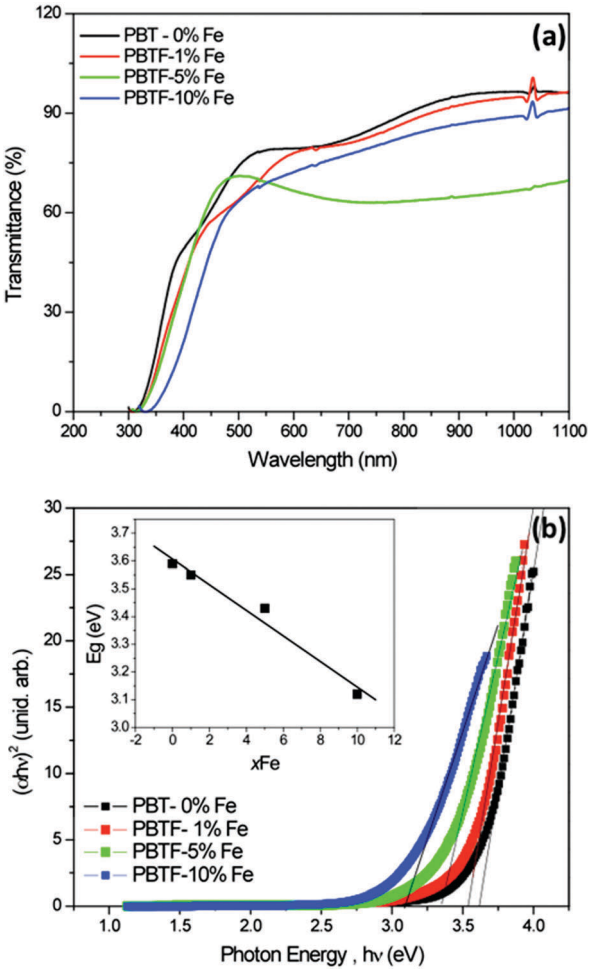

Fig. 2 (a) Optical transmission spectra for the PBT-0, PBTF-1, PBTF-5 and PBTF-10 films on quartz substrates, and (b) $(\alpha h\nu)^2$ *versus* ($h\nu$) for the thin films on quartz substrates. The optical band gap energy E_g was obtained by extrapolation of the linear region for $(\alpha h\nu)^2 = 0$. The inset of (b) show the variation of band gap energies with increasing Fe doping content.

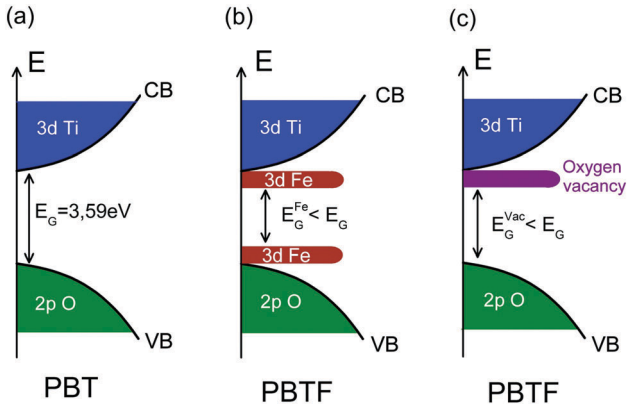

Fig. 3 (a) Simplified band diagram for the PBT thin films. The band gap was estimated using Tauc's law. Band gap narrowing due to Fe doping and the presence of vacancies is represented in panels (b) and (c), respectively.

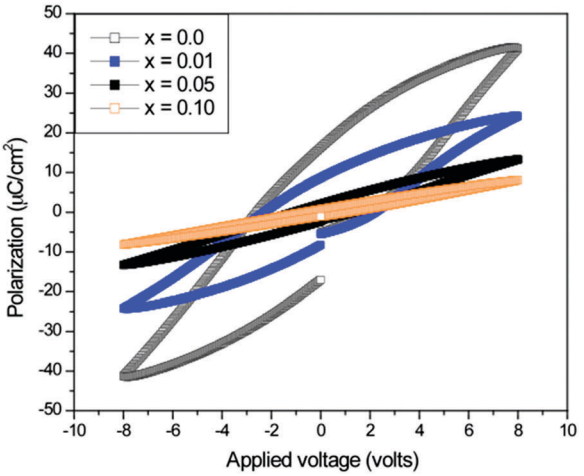

Fig. 4 Typical hysteresis loops for the $Pb_{0.50}Ba_{0.50}Ti_{1-x}Fe_xO_3$ thin films on $Si/SiO_2/Ti/Pt$ substrates measured at room temperature.

presence of impurity states due to oxygen vacancies $(V_O^{\bullet\bullet})$ and Fe 3d doping plays an important role in the formation of the band structure; when combined, these two factors lead to the introduction of localized energy bands in the original band gap of the undoped PBT sample. These localized states induced by Fe doping are expected to form deep and/or shallow levels, therefore playing a crucial role in lowering the band gap energy. Perovskites can exhibit semiconducting or metallic character, depending on the presence of defects (mainly oxygen vacancies) or doping. Oxygen vacancies act as donor centers, resulting in n-type semiconductors with the Fermi level near the bottom of the CB. Fig. 3 shows a representation of the electronic configuration of the undoped PBT and doped PBTF thin films in the presence of doping or vacancies. There is a band gap narrowing in both cases, but we believe that the Fe-doped samples should present a lower band gap due to the contribution of the Fe orbitals to both VB and CB. A similar optical band gap behavior was reported by Yang *et al.* for $Ba(Ti_{1-x}Ni_x)O_3$ thin films.[37] A strong dependency of the optical band gap with the Ti/Ni ratio was revealed. Several researchers have observed a decrease in the optical band gap by increasing the transition metal doping.[38–40] In addition, there is an approximately linear correlation between the band gap energy and the Fe doping concentration (inset of Fig. 2(b)), similar to that observed for classical semiconductor alloys.[41]

In order to study the role of Fe content in the modification of the ferroelectric properties of the undoped PBT and doped PBTF thin films, macroscopic ferroelectric hysteresis loops were recorded at room temperature using a metal–ferroelectric–metal configuration. The thicknesses of the $Pb_{0.50}Ba_{0.50}Ti_{1-x}Fe_xO_3$ films were 300, 260, 260, and 260 nm for x = 0.0, 0.01, 0.05, and 0.10, respectively. The macroscopic hysteresis loops shown in Fig. 4 indicate a tendency toward the non-ferroelectric (paraelectric) state with increasing Fe content; the P_r values decreased significantly as the Fe concentration increased from x = 0.0 to 0.10. At x = 0.0, 0.01, 0.05, and 0.10, P_r was 16.2, 9.5, 1.8, and 0.8 μC cm^{-2}, respectively. This behavior may be attributed to the following: (i) the phase transition tendency from tetragonal to pseudocubic at room temperature; (ii) the small level of lattice distortion that weakened the electric polarization vector; (iii) when the Fe doping level is lower than 0.05, the acceptor-type Fe doping substitution for B-site ions in the lattice should result in a

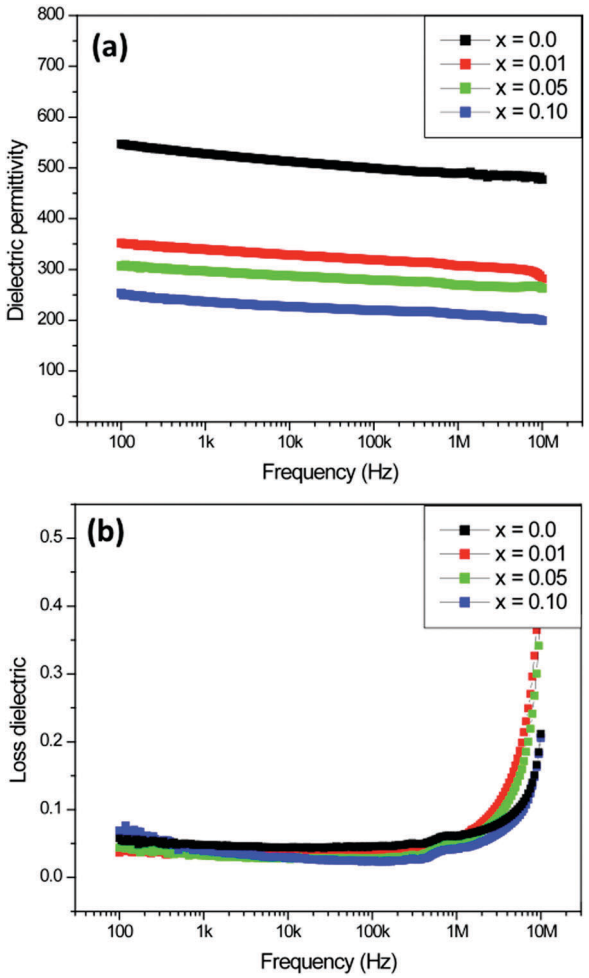

Fig. 5 Frequency dependence of the (a) dielectric permittivity, and (b) dielectric loss for the $Pb_{0.50}Ba_{0.50}Ti_{1-x}Fe_x$ thin films.

significant increase in defect concentration, composed mainly of extrinsic oxygen vacancies, which in turn, results in a significant decrease in the P_r values ($V_O^{\bullet\bullet}$ pins the domain wall motion).

Fig. 5(a) and (b) show the frequency dependence of the dielectric permittivity and dielectric loss, ranging from 10^2 to 10^7 Hz, for the undoped PBT and doped PBTF thin films, measured at room temperature. All thin films showed a gradual decrease in the dielectric permittivity for higher frequencies. The same behavior has been reported for some ferroelectric perovskite thin films.[42,43] The results also show that the dielectric permittivity response decreases significantly, as the Fe doping level increases. The dielectric permittivity and dielectric loss values measured at a frequency of 100 kHz were 499, 319, 279, 219 and 0.045, 0.033, 0.027 and 0.024 for the x = 0.0, 0.01, 0.05 and 0.10 thin films, respectively. It is commonly known that the dielectric permittivity of ferroelectric perovskite thin films is strongly affected by various factors, such as grain size, crystallinity, microstructure, defects (oxygen and metal vacancies), and composition. A possible explanation for the dielectric permittivity decrease with increasing Fe doping concentration may be attributed to: (i) the intrinsic oxygen vacancies that normally occur in the $ABO_{3-\delta}$ perovskite-family structure (eqn (2)), and (ii) when the doping ion contains a lower valence than that of the ion at the B-site, extrinsic oxygen vacancies with positive charges occur (eqn (3)).

$$O_O^{\times} \leftrightarrow V_O^{\bullet\bullet} + 2e' + 1/2O_{2(g)} \quad (2)$$

$$2Fe_{Ti}^{\times} \leftrightarrow 2Fe_{Ti}^{'} + V_O^{\bullet\bullet} + 1/2O_{2(g)} \quad (3)$$

In this approach, the extrinsic oxygen vacancies of the doped PBTF films may exceed the intrinsic ones, due to a higher Fe concentration in the perovskite phase structure; hence, the excess of extrinsic oxygen vacancies can have a negative effect on the dielectric properties. In contrast, when Fe^{3+} substitutes for Ti^{4+}, $Fe_{Ti}^{'}$ extrinsic defects behave as electron acceptors in the perovskite structure and they can effectively reduce the dielectric loss.

Fig. 6 shows the room temperature dielectric permittivity of the thin films, measured at 100 kHz, as a function of the applied voltage. For the undoped PBT thin films the curves are butterfly-shaped, indicating the presence of a switchable domain structure (ferroelectric domains). For the doped PBTF thin films, it is clear that the hysteretic behavior is remarkably reduced upon addition of Fe; this result suggests tetragonal ferroelectric phase instability, associated with a weakened or suppressed short- and long-range ferroelectric dipolar ordering,

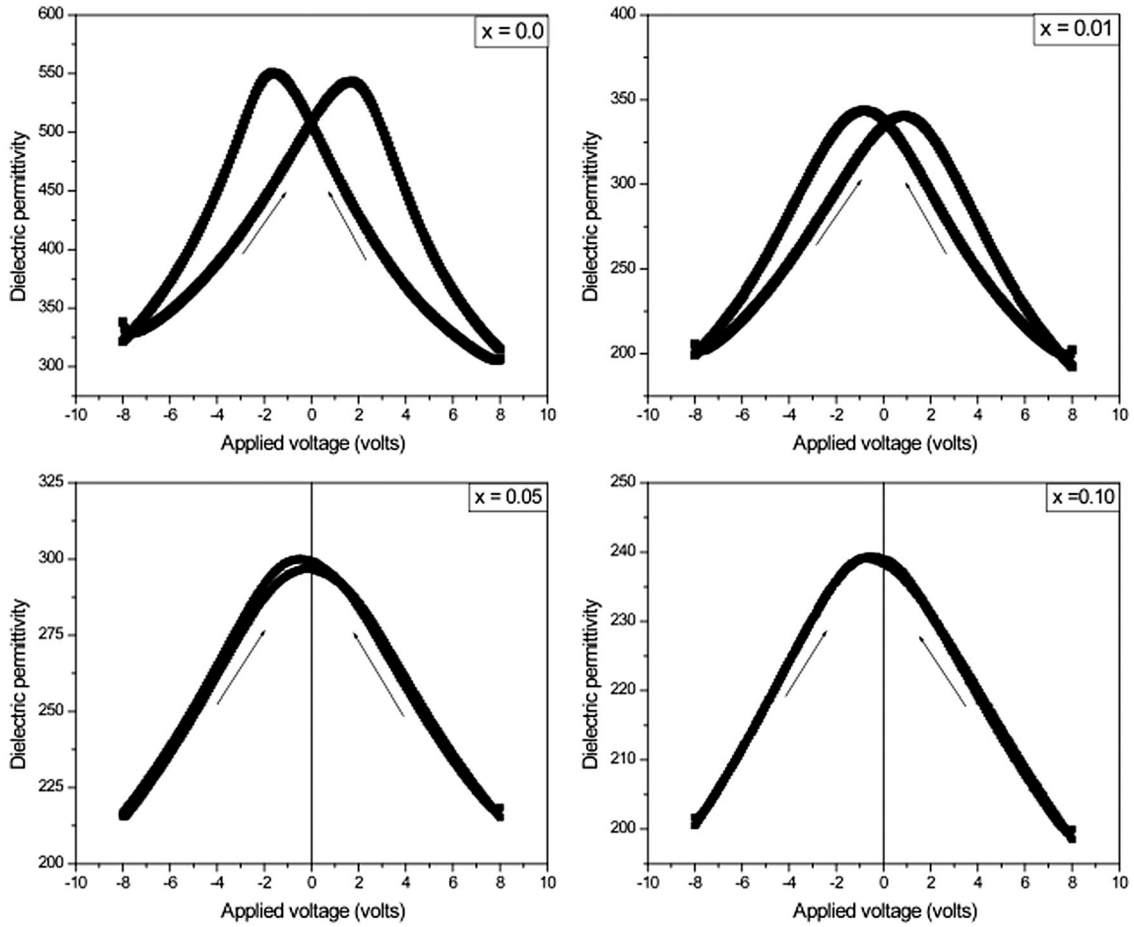

Fig. 6 Typical dielectric permittivity *versus* applied voltage curves at 100 kHz for the $Pb_{0.50}Ba_{0.50}Ti_{1-x}Fe_xO_3$ thin films with x = 0.0, 0.01, 0.05, and 0.10.

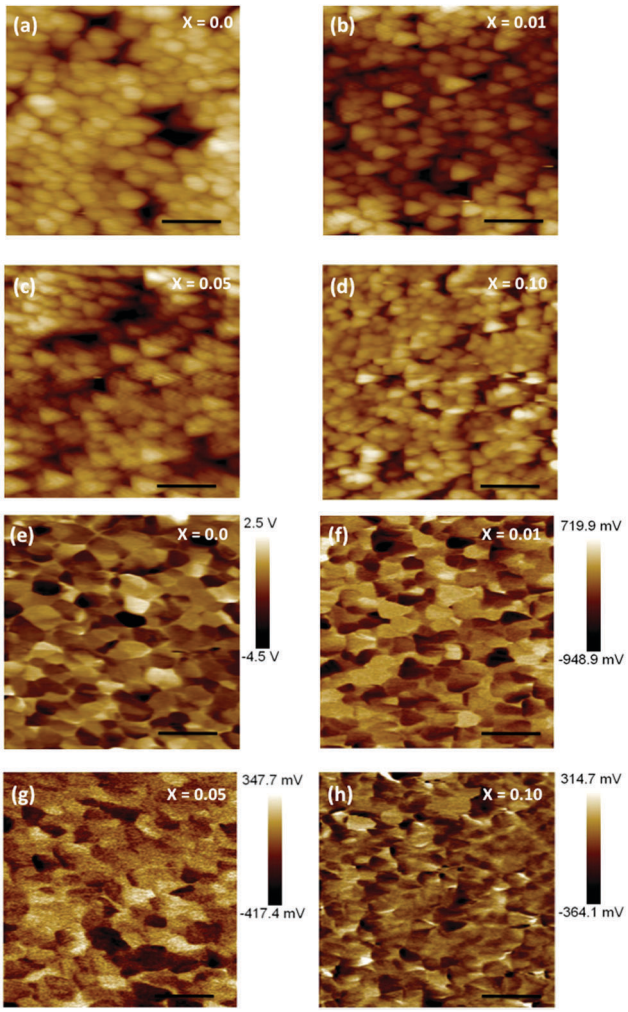

Fig. 7 (a–d) Topography and (e–h) out-of-plane PFM images of the $Pb_{0.50}Ba_{0.50}Ti_{1-x}Fe_xO_3$ thin films for x = 0.0, 0.01, 0.05, and 0.10. The bar in the topography and PFM images represents 500 nm. The scan sizes are 2 μm × 2 μm.

due to tetragonal structural frustration (lower level of lattice distortion). In addition, when x = 0.10, the lattice distortion level is very small and the curves are superimposed, exhibiting a non-ferroelectric behavior. Therefore, these results are in good agreement with the interpretation of both Raman and XRD results. Although, the overall results suggest non-ferroelectric behavior as the Fe content is further increased, we cannot exclude the possibility of weak ferroelectricity associated with the existence of small polar nanoregions, due to compositional disorder.

For this purpose, the PFM[44–47] technique provides some insight into the domain structure modifications observed during chemical doping/substitution at the nanoscale level. Fig. 7 shows both surface topography and out-of-plane (OP-PFM) piezoresponse images of the films with different Fe content. The investigation of the surface topography revealed that the average grain size gradually decreased with increasing Fe content, as shown in Fig. 7(a)–(d). In addition, as the Fe content increased from 0 to 10 mol% the average grain size decreased

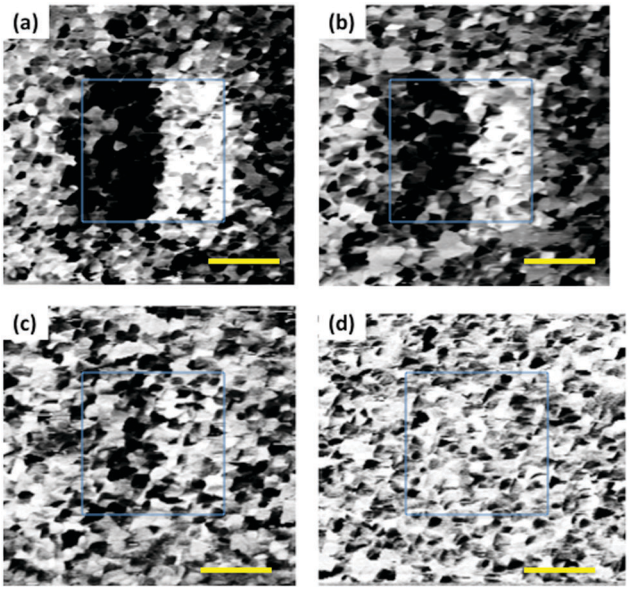

Fig. 8 Square pattern "writing" for the $Pb_{0.50}Ba_{0.50}Ti_{1-x}Fe_xO_3$ thin films with a DC voltage of ±12 V (2 × 2 μm^2): (a) x = 0.0, (b) x = 0.01, (c) x = 0.05, and (d) x = 0.10. The bar in the PFM images represents 1 μm.

from 115 to 55 nm. The piezoelectric performance as a function of the Fe content is shown in Fig. 7(e)–(h). Out-of-plane piezoresponse images of the surface of the x = 0.0 and 0.01 thin films revealed highly contrasted PFM images, as shown in Fig. 7(e) and (f), respectively. These contrasts are a clear signature of a ferroelectric domain structure oriented along different directions, *i.e.*, the dark regions represent domains with downward polarization vectors, while the bright regions represent domains with upward polarization vectors. Dark or bright regions of intermediate intensity correspond to other orientations. Hence, this suggests a polycrystalline nature, where the domain structures are randomly oriented. In addition, the featured sizes in surface topography and the magnitude of the piezoresponse image are comparable, suggesting that most

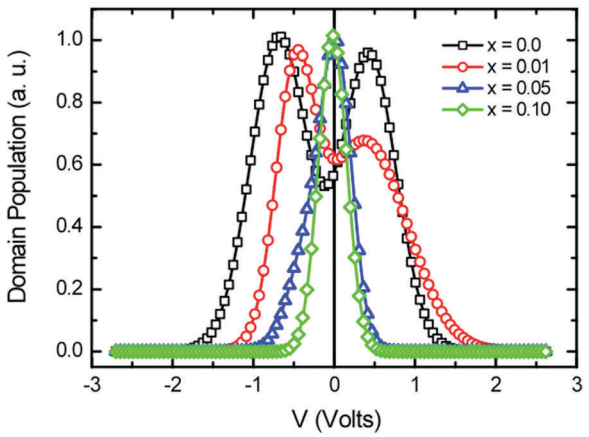

Fig. 9 Piezoresponse variation histogram for the $Pb_{0.50}Ba_{0.50}Ti_{1-x}Fe_xO_3$ thin films after poling with ±12 V. It consists of three distributions: domains with positive, negative, and zero piezoresponses.

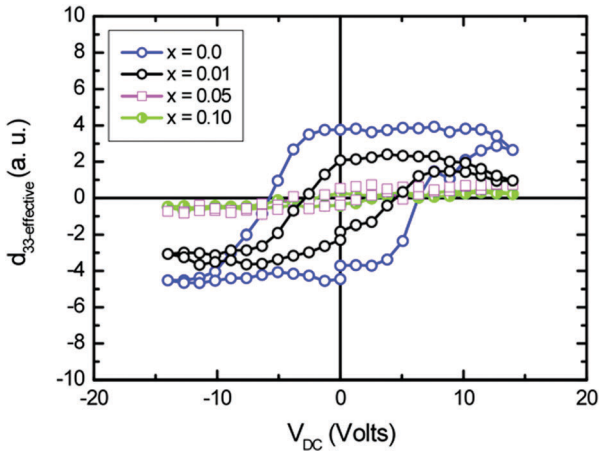

Fig. 10 Local piezoresponse hysteresis loops for the $Pb_{0.50}Ba_{0.50}Ti_{1-x}Fe_xO_3$ thin films from an individual grain for x = 0.0, 0.01, 0.05, and 0.10.

of the domain structures are limited by the grain size of the thin films.

A further increase of the Fe content to x = 0.05 and 0.10 significantly influences the domain structure, as shown in Fig. 7(g) and (h), respectively. Weak domain structures are also observed, as indicated by the low-signal piezoresponse images (regions with nearly zero piezoresponse). This confirms the weak or even suppressed piezo/ferroelectricity behavior, accompanied by a ferroelectric–paraelectric phase transition at room temperature. These experimental observations are completely consistent with the substitution of Ti ions for Fe ions (XRD and Raman experimental data). Substitution of Ti ions with Fe ions decreases the off-center displacement of the Ti ions inside the octahedral oxygen cage; this weakens the interaction between short- and long-range electric dipolar moments and produces a weak or suppressed piezo/ferroelectricity behavior, accompanied by ferroelectric–paraelectric phase transition at room temperature, as confirmed by the Raman and XRD results. Sun *et al.*[42] reported similar results for $Bi_{1-x}Sm_xFeO_3$ thin films (x = 0.0, 0.05, 0.10, and 0.15) grown on $Si/SiO_2/Ti/Pt$ substrates using a sol–gel method.

In order to investigate localized polarization switching behaviors for the undoped PBT and doped PBTF thin films, a

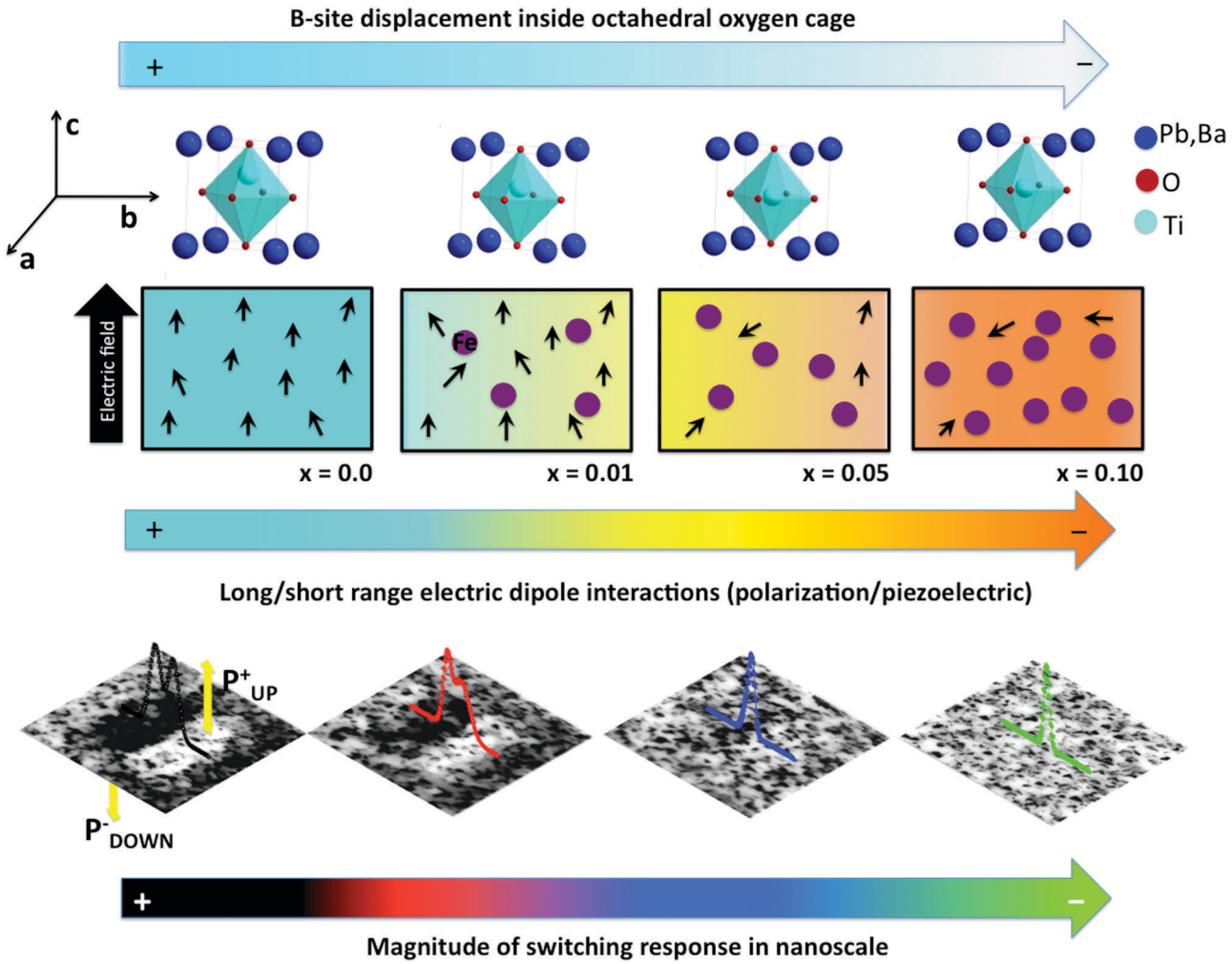

Fig. 11 Schematic illustration of the electric dipole and polarization switching evolution process for the PBTF thin films, depending on the Fe concentration (x), where the effects of the B-site displacement and strength of long- and short-range electric dipole interactions on the electric field are key factors.

DC bias was applied to the conducting PFM-tip probe while scanning the desired area. Local poling ("writing") was achieved on a square-shaped region (2 μm × 2 μm, solid blue line) by alternately applying a DC voltage of −12 V (black contrast) and +12 V (bright contrast) to the conductive PFM-tip, corresponding to downward and upward polarization stable states, respectively. This approach is illustrated in Fig. 8. After applying a DC voltage of −12 V (dark contrast) and then +12 V (bright contrast), strong domain patterns are clearly visible on the PFM images shown in Fig. 8(a) and (b); this indicates that the local polarization vector direction can be switched, therefore showing that both x = 0.0 and 0.01 thin films support ferroelectric behavior at room temperature, as depicted in Fig. 8(a) and (b), respectively. On the other hand, the "writing" pattern is significantly modified for the x = 0.05 and 0.10 thin films (Fig. 8(c) and (d), respectively). It should be noted that both thin films show low contrast after applying a voltage of −12 V (dark contrast) and then +12 V (bright contrast), indicating that the polarization of the films is irreversible under the applied electric voltages (non-switchable polarization). This can be attributed to a deterioration of the tetragonal ferroelectric structural phase, accompanied by domain wall pinning, as the amount of Fe increased at room temperature. To further investigate the piezoelectric properties, we carried out a statistical analysis of the domain distribution, represented by standard histograms, known as piezohistograms. Fig. 9 shows the piezohistogram of the $Pb_{0.50}Ba_{0.50}Ti_{1-x}Fe_xO_3$ thin films with different compositions, acquired from the piezoresponse images after the poled state represented in Fig. 8. For the x = 0.0 and 0.01 films, the piezohistogram response revealed a typical well-developed butterfly-like shape, corresponding to a large relative population of positive (upward) and negative (downward) domains. As the Fe content increased, the difference between positive domains and negative peak positions decreased, and overlapping peaks for x = 0.05 and 0.10 were observed; the domain population decreased noticeably towards the absence of two opposite stable states, indicating an irreversible process. These results are in good agreement with those shown in Fig. 6. However, we observed that when x = 0.0 and 0.01, the maximum intensity of positive and negative domain distributions was asymmetrical. It has been reported that this asymmetry phenomenon is a result of self-polarization effects, work function differences between the PFM-tip and the bottom electrodes, space-charge effects, and oxygen vacancy defects ($V_O^{\bullet}$ or $V_O^{\bullet\bullet}$).[22,42,48–51]

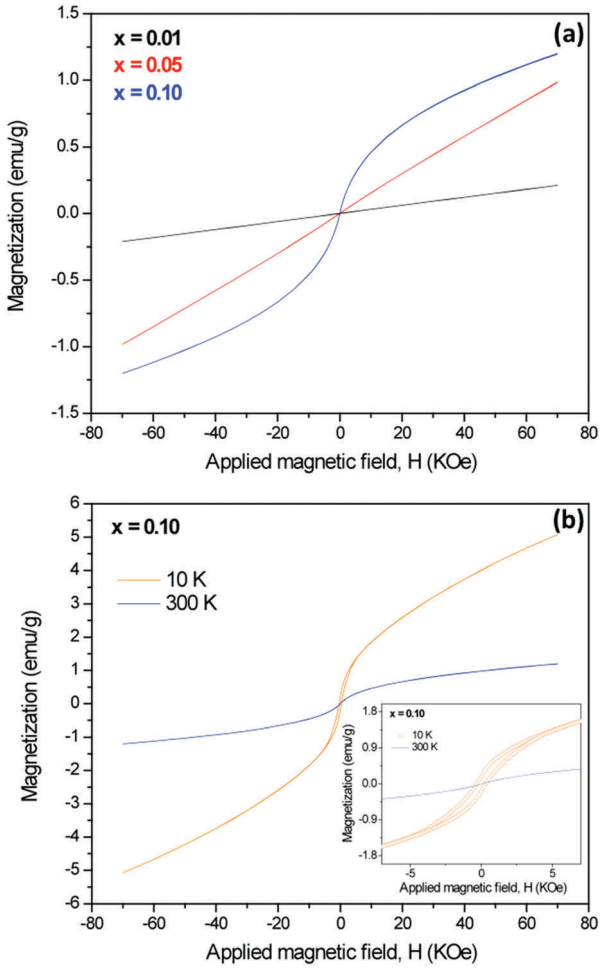

Fig. 12 (a) Room temperature M–H magnetic hysteresis loops for the $Pb_{0.50}Ba_{0.50}Ti_{1-x}Fe_xO_3$ samples investigated with different Fe contents, and (b) M–H magnetic hysteresis loops for the samples with x = 0.10 at 10 and 300 K. The inset shows a magnification around the origin.

In addition, other typical signatures of reversible domain switching are the local piezoelectric hysteresis loops measured on a single grain. As shown in Fig. 10, the local piezoelectric hysteresis loops decrease significantly with increasing Fe content. In addition, the undoped PBT thin films show a well-defined and saturated piezoelectric hysteresis loop, suggesting a high tetragonal distortion at the nanoscale level. When x = 0.01, the doped PBTF thin films also show a local piezoelectric hysteresis loop, which is further evidence supporting the ferroelectric behavior of the films, but their piezoelectric response was weak, due to the reduced tetragonal distortion. On the other hand, by increasing the Fe content to x = 0.05, the piezoelectric response decayed significantly, producing slimmer hysteresis loops. This can be attributed to a much lower tetragonal distortion (c/a ratio), which weakens the short and long-range electric dipole displacement (polarization) of the Ti atoms inside the oxygen octahedral cage, as revealed by the XRD and Raman measurements. Fig. 11 shows a diagram where the electric polarization evolution of the thin films evidenced a weakened distortion of the TiO_6 sublattice and displacement along the polar axis (polarization) when the Fe content increased. For the undoped PBT thin films, the tetragonal structure, which is favored regarding long-range interactions, presents an alignment of all the dipoles. As the Fe content increases, the tetragonality decreases, thus leading to a negative effect on the displacement along the polar axis (B-site), which decreases the electric polarization, due to an insufficient number of electric dipoles.

To further characterize the samples, we measured the magnetic properties of powder samples with the same composition, as shown in Fig. 12(a). As observed in Fig. 12(a), the M–H curves reveal only linear correlations for the samples with Fe content of x = 0.01 and 0.05. This indicates either missing or

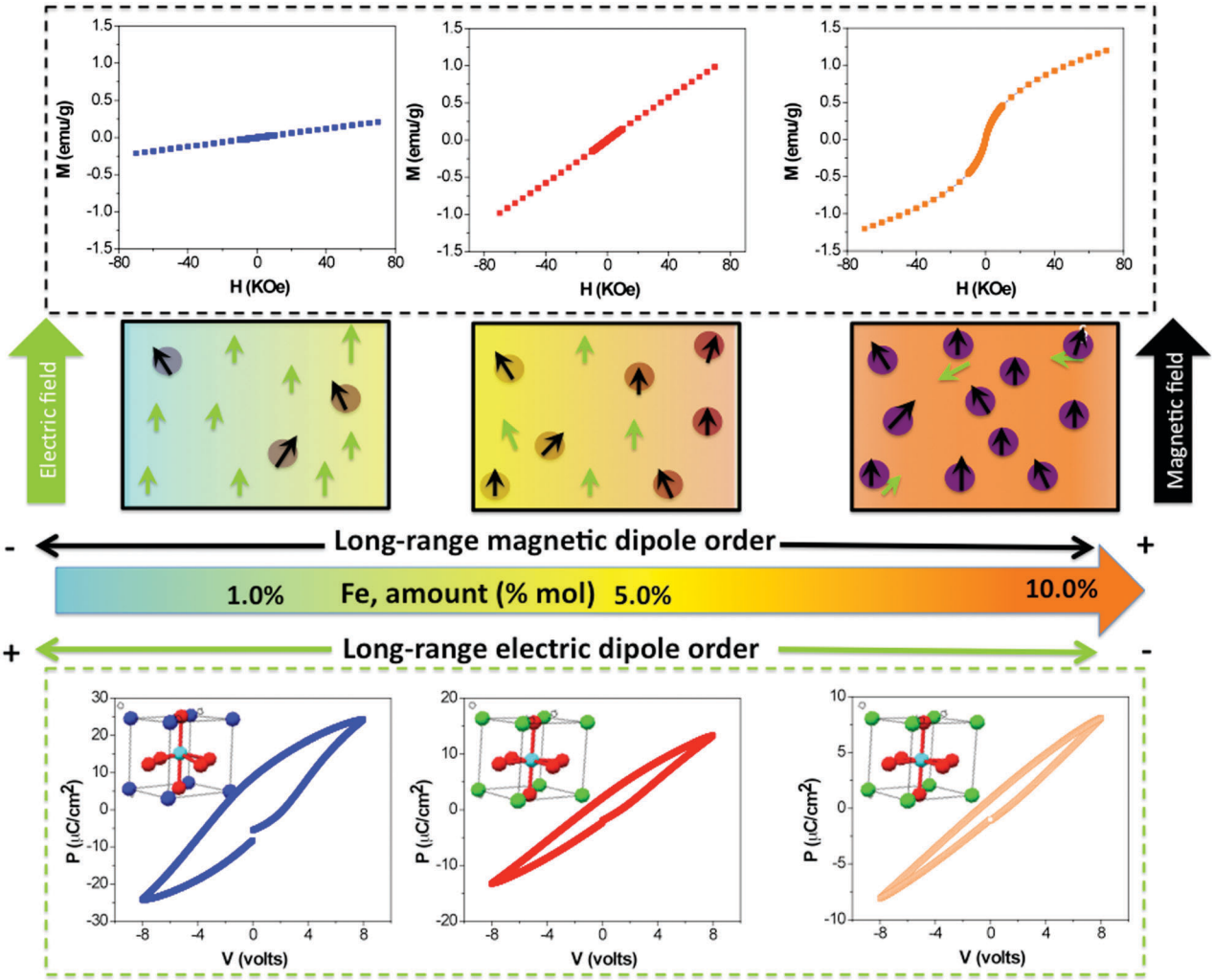

Fig. 13 Schematic illustration of the long-range magnetic order evolution process *versus* long-range electric polarization order evolution process for the PBTF samples, depending on the Fe concentration (mol%), showing that the polarization and magnetization behaviors evolve in opposite directions. In this case, the key factor is the B-cation displacement and magnetic cation amount, providing a path for magneto-electric field coupling in multiferroic materials. The inset show the TiO_6 octahedral distortion.

low, long-range magnetically ordered state interactions between the Fe^{3+} spins, *i.e.*, a purely paramagnetic behavior. However, for the sample with $x = 0.10$, the M–H curve shows a typical S-shaped hysteresis loop, indicating some long-range magnetically ordered states (ferromagnetic interactions) at room temperature. Ferromagnetic properties have been reported as well for the Fe-doped $PbTiO_3$ and $Pb_{0.7}Sr_{0.3}Fe_{0.012}Ti_{0.988}O_3$ samples prepared using different techniques.[6,52,53] In addition, Fig. 12(b) shows a narrow magnetic loop, measured at 10 K, for the sample where $x = 0.10$, with a coercive field of 300 Oe, characteristic of a magnetically soft material. The magnetic signal response increased significantly with decreasing temperature, due to the thermal fluctuation suppression of the magnetic dipoles. In addition, magnetic hysteresis loop patterns clearly demonstrate no signs of saturation, even for a field as high as 70 000 Oe (7 Tesla), which indicates that the ferromagnetic interactions are weak even at low temperature, thus leading to the weak ferromagnetic nature of the sample.

Our results show that a reduction in the ferroelectric properties associated with the presence of Fe coincides with the appearance of a magnetic response, indicating the existence of a long-range magnetic ordering. Therefore, for the doped PBTF system, the magnitude of the off-centered ions inside the octahedral oxygen cage, which is a key factor for the electric polarization, decreased towards a centrosymmetric perovskite structure, resulting in a reduction and/or disappearance of the electric dipoles, thus affecting the magneto-electric coupling, as schematically illustrated in Fig. 13.

Conclusions

Several $Pb_{0.50}Ba_{0.50}Ti_{1-x}Fe_xO_3$ polycrystalline thin films ($x = 0.0$, 0.01, 0.05, and 0.10) were prepared on Pt(111)/Ti/SiO_2/Si and quartz substrates using a chemical solution deposition method. Through a multi-technique approach, we showed both

a weakened distortion of the TiO_6 sublattice and a decrease of the ferroelectric and piezoelectric responses. Notwithstanding, XRD analysis revealed an average cubic-type structural phase for the composition above $x = 0.01$; the presence of Raman-active modes after the phase transition at room temperature indicated a short-range structural disorder. Therefore, the thin films showed a tetragonal to pseudocubic-type structural phase transition when the Fe content increased. The optical band gap was also affected by the increase of the Fe content: it decreased from 3.59 to 3.12 eV, which was probably due to the inclusion of localized states in the forbidden band energy. Fe addition also induced variations at different scales, causing a gradual modification of the domain structure, as clearly observed on the PFM results. For low Fe doping compositions, the PFM images revealed both localized piezoelectric contrast and domain switching, in accordance with the macroscopic investigations.

Moreover, well-saturated, local piezo-hysteresis loops on a single grain were observed for the undoped PBT thin films, while they were almost suppressed in the Fe-doped samples due to the absence of short and long-range polar ordering. Finally, a phase transition from paramagnetic to ferromagnetic with increasing Fe content was observed. Therefore, our results suggest that short and long-range structural order–disorder effects, caused when a Fe ion replaced a Ti ion inside the octahedral oxygen cage, play an important role in reducing the tetragonal distortion; in addition, the piezo/ferroelectric response is expected to disappear, as opposed to the long-range magnetic order that increases progressively.

Acknowledgements

This study was financially supported by the Brazilian agencies FAPESP and CNPq. We would like to thank CEPID/CMDMC/INCTMN/CDMF, FAPESP (processes no. 11/20536-7, 12/14106-2, and 13/07296-2), CNPq (process no. 470147/2012-1), and Squid-UFSCAR_QD_MPMS3 – FAPESP (process no. 09/54082-2).

References

1 Q. Zhang, D. Sando and V. Nagarajan, *J. Mater. Chem. C*, 2016, **4**, 4092.
2 M.-X. Zhou, B. Chen, H.-B. Sun, J.-G. Wan, Z.-W. Li, J.-M. Liu, F.-Q. Song and G.-H. Wang, *NANO*, 2014, **24**, 225702.
3 S. Habouti, C.-H. Solterbeck and M. Es-Souni., *J. Appl. Phys.*, 2007, **102**, 074107.
4 H. Zhao, J. Miao, L. Zhang, Y. Rong, J. Chen, J. Deng, R. Yu, J. Cao, H. Wang and X. Xing, *Dalton Trans.*, 2016, 1554.
5 L. Zhang, J. Chen, H. Zhao, L. Fan, Y. Rong, J. Deng, R. Yua and X. Xing, *Dalton Trans.*, 2013, 585.
6 C. Sun, J. Wang, H. Kang, J. Chen, M. J. Kimb and X. Xing, *Dalton Trans.*, 2010, 9952.
7 S. A. Ivanov, R. Tellgren, F. Porcher, T. Ericsson, A. Mosunov, P. Beran, S. K. Korchagina, P. Anil Kumar, R. Mathieu and P. Nordblad, *Mater. Res. Bull.*, 2012, **47**, 3253.
8 B. Fraygola, A. A. Coelho, D. Garcia and J. A. Eiras, *Process. Appl. Ceram.*, 2012, **6**, 65.
9 M. Borah and D. Mohanta, *J. Mater. Res.*, 2012, **27**, 2965.
10 I. Grinberg, D. V. West, M. Torres, G. Gou, D. M. Stein, L. Wu, G. Chen, E. M. Gallo, A. R. Akbashev, P. K. Davies, J. E. Spanier and A. M. Rappe1, *Nature*, 2013, **503**, 509.
11 A. R. B. M. Yusoff and M. K. Nazeeruddin, *J. Phys. Chem. Lett.*, 2016, **7**, 851.
12 H. Wang, J. Wen, D. J. Miller, Q. Zhou, M. Chen, H. N. Lee, K. M. Rabe and X. Wu, *Phys. Rev. X*, 2016, **6**, 011027.
13 D. Chen, C. Chen, Z. Zhang, Z. M. Baiyee, F. Ciucci and Z. Shao, *ACS Appl. Mater. Interfaces*, 2015, **7**, 8562.
14 G. Dong, H. Fan, H. Tian, J. Fang and Q. Li, *RSC Adv.*, 2015, **5**, 29618.
15 V. Fuflyigin, F. Wang, H. Jiang, J. Zhao and P. Norris, *Appl. Phys. Lett.*, 2000, **76**, 1641.
16 C. T. Lee, M. S. Zhang and Z. Yin, *J. Mater. Sci.*, 2008, **43**, 2675.
17 O. A. Tyablikov, D. Batuk, A. A. Tsirlin, M. Batuk, V. Yu. Verchenko, D. S. Filimonov, K. V. Pokholok, D. V. Sheptyakov, M. G. Rozova, J. Hadermann, E. V. Antipov and A. M. Abakumov, *Dalton Trans.*, 2015, 10753.
18 J. A. Brehm, H. Takenaka, C.-W. Lee, I. Grinberg, J. W. Bennett, M. R. Schoenberg and A. M. Rappe, *Phys. Rev. B: Condens. Matter Mater. Phys.*, 2014, **89**, 195202.
19 H. Zhao, J. Wang, L. Zhang, Y. Rong, J. Chen, K. Ibrahim and X. Xing, *Dalton Trans.*, 2013, 10358.
20 H. Ren, G. Xu, X. Wei, Y. Liu, X. Hou, P. Du, W. Weng, G. Shen and G. Han, *Appl. Phys. Lett.*, 2007, **91**, 063106.
21 W. Bai, X. J. Meng, T. Lin, L. Tian, C. B. Jing, W. J. Liu, J. H. Ma, J. L. Sun and J. H. Chu, *J. Appl. Phys.*, 2009, **106**, 124908.
22 A. Wu, P. M. Vilarinho, V. V. Shvartsman, G. Suchaneck and A. L. Kholkin, *NANO*, 2005, **16**, 2587.
23 A. Bayart, Z.-M. Shao, A. Ferri, P. Roussel, R. Desfeux and S. Saitzek, *RSC. Adv.*, 2016, **6**, 32994.
24 N. Panwar, I. Coondoo, A. Tomar, A. L. Kholkin, V. S. Puli and R. S. Katiyar, *Mater. Res. Bull.*, 2012, **47**, 4240.
25 V. A. Khomchenko, D. A. Kiselev, J. M. Vieira, L. Jian, A. L. Kholkin, A. M. L. Lopes, Y. G. Pogorelov, J. P. Araujo and M. Maglione, *J. Appl. Phys.*, 2008, **103**, 024105.
26 N. Balke, P. Maksymovych, S. Jesse, A. Herklotz, A. Tselev, C.-B. Eom, I. I. Kravchenko, P. Yu and S. V. Kalinin, *ACS Nano*, 2015, **6**, 6484.
27 M. C. Ferrarelli, C. C. Tan and D. C. Sinclair, *J. Mater. Chem.*, 2011, **21**, 6292.
28 S. Mo Yang, J.-G. Yoon and T. W. Noh, *Curr. Appl. Phys.*, 2011, **11**, 1111.
29 D. Gobeljic, V. V. Shvartsman, A. Belianinov, B. Okatan, S. Jesse, S. V. Kalinin, C. Groh, J. Rödelc and D. C. Lupascu, *Nanoscale*, 2016, **8**, 2168.
30 Q. Yu, J.-F. Li, F.-Y. Zhua and J. Li, *J. Mater. Chem. C*, 2014, **2**, 5836.
31 K. C. Verma, R. K. Kotnala and N. S. Negi, *Appl. Phys. Lett.*, 2008, **92**, 152902.
32 H. Ganegoda, J. A. Kaduk and C. U. Segre, *Powder Diffr.*, 2013, **28**, 254.

33 M. Imada, A. Fujimori and Y. Tokura, *Rev. Mod. Phys.*, 1998, **70**, 1039.
34 J. D. Freire and R. S. Katiyar, *Phys. Rev. B: Condens. Matter Mater. Phys.*, 1998, **37**, 2074.
35 K. I. Doig, J. J. P. Peters, S. Nawaz, D. Walker, M. Walker, M. R. Lees, R. Beanland, A. M. Sanchez, C. F. McConville, V. R. Palkar and J. Lloyd-Hughes, *Sci. Rep.*, 2015, **5**, 7719.
36 D. L. Wood and J. Tauc, *Phys. Rev. B: Condens. Matter Mater. Phys.*, 1972, **5**, 3144.
37 J. Yang, T. Zhang, M. Ni, L. Ding and W. F. Zhang, *Appl. Surf. Sci.*, 2009, **256**, 17.
38 Z. Ting, Y. Jiang, D. L. Hong and Z. W. Feng, *Chin. Phys. B*, 2013, **11**, 117801.
39 Y. W. Li, J. L. Sun, X. J. Meng, J. H. Chu and W. F. Zhang, *Appl. Phys. Lett.*, 2004, **85**, 1964.
40 N. V. Dang, H. M. Nguyen, P. Y. Chuang, T. D. Thanh, V. D. Lam, C. H. Lee and L. V. Hong, *Chin. J. Phys.*, 2012, **50**, 262.
41 E. F. Schubert, *Doping in III-V semiconductors*, Cambridge University Press, Cambridge, 1993.
42 W. Sun, J.-F. Li, Q. Yu and L.-Q. Cheng, *J. Mater. Chem. C*, 2015, **3**, 2115.
43 N. Ortega, A. Kumar, R. S. Katiyar and C. Rinaldi, *Thin Solid Films*, 2010, **519**, 641.
44 N. Horchidan, A. C. Ianculescu, C. A. Vasilescu, M. Deluca, V. Musteata, H. Ursic, R. Frunza, B. Malic and L. Mitoseriu, *J. Eur. Ceram. Soc.*, 2014, **34**, 3661.
45 S. V. Kalinin, R. Shao and D. A. Bonnell, *J. Am. Ceram. Soc.*, 2005, **88**, 1077.
46 C. Harnagea, M. Azodi, R. Nechache, C.-V. Cojocaru, V. Buscaglia, M. T. Buscaglia, P. Nanni, F. Rosei and A. Pignolet, *Phase Transitions*, 2013, **86**, 635.
47 I. Coondoo, N. Panwar, I. Bdikin, V. S. Puli, R. S. Katiyar and A. L. Kholkin, *J. Phys. D: Appl. Phys.*, 2012, **45**, 055302.
48 L. Zhao, Z. Lu, F. Zhang, G. Tian, X. Song, Z. Li, K. Huang, Z. Zhang, M. Qin, S. Wu, X. Lu, M. Zeng, X. Gao, J. Dai and J.-M. Liu, *Sci. Rep.*, 2015, **5**, 9680.
49 J. Hong, H. W. Song, S. Hong, H. Shin and K. No, *J. Appl. Phys.*, 2002, **92**, 7434.
50 E. C. Lima, E. B. Araujo, A. G. Souza Filho, A. R. Paschoal, I. K. Bdikin and A. L. Kholkin, *J. Phys. D: Appl. Phys.*, 2012, **45**, 215304.
51 A. Ferri, S. Saitzek, A. Da Costa, R. Desfeux, G. Leclerc, R. Bouregba and G. Poullain, *Surf. Sci.*, 2008, **602**, 1987.
52 Z. Ren, G. Xu, X. Wei, Y. Liu, X. Hou, P. Du, W. Weng, G. Shen and G. Han, *Appl. Phys. Lett.*, 2007, **91**, 063106.
53 R. K. Kotnala, K. Chand Verma, M. C. Mathpal and N. S. Negi, *J. Phys. D: Appl. Phys.*, 2009, **42**, 085408.

